Nano Research
2021, 14(6): 1961–1966
ISSN 1998-0124 CN 11-5974/O4
https://doi.org/10.1007/s12274-020-3059-3

Research Article

Intrinsic carrier multiplication in layered Bi_2O_2Se avalanche photodiodes with gain bandwidth product exceeding 1 GHz

Vinod K. Sangwan[1], Joohoon Kang[1,†], David Lam[1], J. Tyler Gish[1], Spencer A. Wells[1], Jan Luxa[2], James P. Male[1], G. Jeffrey Snyder[1], Zdeněk Sofer[2], and Mark C. Hersam[1,3,4] (✉)

[1] *Department of Materials Science and Engineering, Northwestern University, Evanston, IL 60208, USA*
[2] *Department of Inorganic Chemistry, University of Chemistry and Technology Prague, Technicka 5, 166 28 Prague 6, Czech Republic*
[3] *Department of Chemistry, Northwestern University, Evanston, IL 60208, USA*
[4] *Department of Electrical and Computer Engineering, Northwestern University, Evanston, IL 60208, USA*
[†] *Present address: School of Advanced Materials Science and Engineering, Sungkyunkwan University (SKKU), Suwon 16419, Republic of Korea*

Received: 24 June 2020 / **Revised:** 26 July 2020 / **Accepted:** 14 August 2020

ABSTRACT

Emerging layered semiconductors present multiple advantages for optoelectronic technologies including high carrier mobilities, strong light–matter interactions, and tunable optical absorption and emission. Here, metal-semiconductor-metal avalanche photodiodes (APDs) are fabricated from Bi_2O_2Se crystals, which consist of electrostatically bound $[Bi_2O_2]^{2+}$ and $[Se]^{2-}$ layers. The resulting APDs possess an intrinsic carrier multiplication factor up to 400 at 7 K with a responsivity gain exceeding 3,000 A/W and bandwidth of ~ 400 kHz at a visible wavelength of 515.6 nm, ultimately resulting in a gain bandwidth product exceeding 1 GHz. Due to exceptionally low dark currents, Bi_2O_2Se APDs also yield high detectivities up to 4.6×10^{14} Jones. A systematic analysis of the photocurrent temperature and bias dependence reveals that the carrier multiplication process in Bi_2O_2Se APDs is consistent with a reverse biased Schottky diode model with a barrier height of ~ 44 meV, in contrast to the charge trapping extrinsic gain mechanism that dominates most layered semiconductor phototransistors. In this manner, layered Bi_2O_2Se APDs provide a unique platform that can be exploited in a diverse range of high-performance photodetector applications.

KEYWORDS

layered semiconductor, photodetector, high-frequency, Schottky diode, impact ionization

1 Introduction

Layered semiconductors have attracted significant interest for both fundamental and applied optoelectronic research as a result of their excitonic physics, weak electrostatic screening, tunable optical absorption and emission, interlayer interactions, optically accessible topological states, and strong coupling to the environment and neighboring low-dimensional materials [1–7]. Among the many optoelectronic applications for layered semiconductors, photodetectors are particularly prominent [8]. Semiconductor photodetectors involve a two-step process where a photon is captured, and then the resulting electron–hole pair is separated to produce a photocurrent or photovoltage [1, 4, 9–12]. The overall photodetector efficiency depends on the concurrent optimization of multiple materials parameters such as oscillator strength, carrier mobility, doping, and band alignments. For layered semiconductor photodetectors, the most common approach exploits charge trapping in phototransistors via photogating and photovoltaic effects to improve the extrinsic gain, resulting in high responsivities up to 10^7 A/W [1, 2, 4, 9, 12–18]. An alternative approach integrates a high-mobility layered semiconductor with a strong absorber (e.g., quantum dots) in mixed-dimensional heterojunctions, again yielding responsivities on the order of 10^7 A/W [1, 19]. Both approaches, however, suffer from large dark currents, which imply low detectivities, in addition to large capacitances that compromise photodetector speed.

On the other hand, intrinsic carrier multiplication provides a pathway to achieving high gain, speed, and detectivity simultaneously in semiconductor photodetectors. For example, bulk Ge/Si semiconductor avalanche photodiodes (APDs) show unity-gain cutoff frequencies exceeding 300 GHz [20]. In low-dimensional semiconductors, InGaAs/GaAs nanowire APDs can detect single photons with counting rates in excess of 7 MHz [21]. Despite these clear advantages, limited success has been previously reported for carrier multiplication processes in layered semiconductors. One such layered semiconductor, InSe, has been utilized in Schottky diode photodetectors with Al electrodes, resulting in a low multiplication factor (< 50) and large response time (60 μs) at visible wavelengths [22]. Black phosphorus/WS_2 heterojunction-based APDs show even lower gain (~ 2) and slower response (on the order of seconds) [23]. In addition, black phosphorus/InSe heterojunctions provide a ballistic avalanche process with sub-thermionic switching and high gain (~ 10^4), but photodetection is limited to the mid-infrared (wavelength, λ ~ 4 μm) [24]. Although carrier multiplication has been observed in black phosphorus and MoS_2 field-effect transistors, it has only been studied in the context of electrical breakdown, not for photodetectors [25, 26]. Therefore, an opportunity remains for the identification of a layered

Address correspondence to m-hersam@northwestern.edu

semiconductor and corresponding photodetector geometry that exploits intrinsic carrier multiplication for high gain, speed, and detectivity, particularly at visible wavelengths.

Bi_2O_2Se is a layered semiconductor in the diverse class of heteroanionic oxychalcogenides [27–30]. In Bi_2O_2Se, $[Bi_2O_2]^{2+}$ and $[Se]^{2-}$ layers are bonded by electrostatic interactions that are stronger than the van der Waals forces prevalent in other layered materials (Fig. 1(a)) [29]. This bonding motif results in the phenomenon of self-modulation doping, where most of the electron conduction occurs in the bismuth oxide layer that is spatially separated from the selenium atoms that act as dopants, resulting in reduced scattering and thus high mobility up to 10^5 $cm^2/(V·s)$ at 1 K [31, 32]. Furthermore, since the selenium states lie above the conduction band edge, the ionization processes are not thermally activated, and the Bi_2O_2Se band structure is relatively insensitive to physical disorder. While Bi_2O_2Se field-effect transistors possess high room-temperature mobilities (> 100 $cm^2/(V·s)$) and switching ratios (> 10^7), Bi_2O_2Se phototransistors have shown mixed results including a high extrinsic responsivity, $R \sim 10^4$ A/W at $\lambda = 532$ nm, but a slow photoresponse (0.3–7 ms) due to charge trapping [33, 34].

In an effort to more fully exploit the superlative intrinsic optoelectronic properties of Bi_2O_2Se, here we report Bi_2O_2Se APDs with the highest carrier multiplication gain measured to date for a layered semiconductor (~ 400), which results in $R > 10^3$ A/W and an internal quantum efficiency > 10^3 when excited at $\lambda = 515.6$ nm. These devices also show exceptionally low dark currents below 0.2 nA at 7 K, resulting in the highest detectivity (> 10^{14} Jones) reported for a layered semiconductor. Finally, these Bi_2O_2Se APDs possess a photoresponse time of 2.5 μs, which implies a gain bandwidth product exceeding 1 GHz. Through a systematic analysis as a function of lateral applied fields, temperature, and illumination intensity, the carrier multiplication process is elucidated in a manner that provides guidance to future efforts aiming at employing Bi_2O_2Se in optoelectronic technologies.

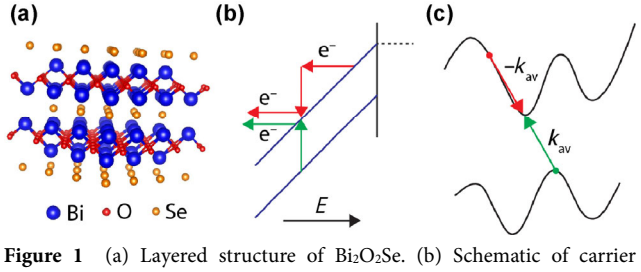

Figure 1 (a) Layered structure of Bi_2O_2Se. (b) Schematic of carrier multiplication in the avalanche process where the excess kinetic energy of a hot electron is used for inter-band excitation of an additional electron–hole pair. (c) Schematic of the hot carrier relaxation in an indirect bandgap semiconductor with nested energy band diagrams conserving both energy and momentum through impact ionization.

2 Results and discussion

The large fields required for the avalanche process are achieved in depletion regions formed either in p-n junction diodes or metal-semiconductor-metal (MSM) Schottky diodes. Schottky diodes have the benefit of minimal semiconductor processing requirements, which is especially relevant for layered semiconductors where traditional approaches of substitutional doping present significant tradeoffs (e.g., compromised charge carrier mobility). The resulting high fields in the depletion region of a reverse-biased Schottky junction drive the charge carriers to gain kinetic energy that can generate additional electron–hole pairs through impact ionization (Fig. 1(b)), resulting in carrier multiplication. The original charge carriers can be injected electrically from the contacts (avalanche breakdown) or through optical excitation (avalanche photocurrent). When electrons are the majority charge carriers (as is the case for Bi_2O_2Se), the multiplication process can be described by $1 - 1/M_n = \int_0^w \alpha_n(E) \cdot \exp\left(-\int_0^x (\alpha_n(E) - \alpha_p(E))dx'\right)dx$, where M_n is the multiplication factor, w is the width of the depletion region, and α_n and α_p are the ionization rates of electrons and holes, respectively [10, 35–37]. As impact ionization requires conservation of both energy and momentum, indirect semiconductors like Bi_2O_2Se are preferred since an offset in band extrema allows hot carriers to relax from a wider range of wavevectors (Fig. 1(c)) [38–40]. In addition, optically excited hot carriers can directly generate electron–hole pairs without an electric field if the excitation energy is larger than twice the bandgap (Bi_2O_2Se bandgap ~ 0.8 eV) [38, 40].

Bi_2O_2Se APDs were fabricated by first isolating small crystals (roughly 0.5 mm × 2 mm) by blade cleavage from a larger bulk Bi_2O_2Se sample that was grown via chemical vapor transport (see Methods section). Transmission electron microscopy (TEM) and selected area electron diffraction (SAED) confirm the crystal structure of Bi_2O_2Se with the expected lattice constant of 0.28 nm (Fig. 2) [28]. High-angle annular dark-field (HAADF) and X-ray photoelectron spectroscopy (XPS) further confirm the stoichiometry of the Bi_2O_2Se crystals (see Figs. S1 and S2 in the Electronic Supplementary Materials (ESM)). The Au electrodes (thickness ~ 50 nm) were evaporated through TEM grids as a shadow mask to define a channel length and width of 5 and 30 μm, respectively. Crystal handling and metal evaporation were conducted inside a N_2 glove box to minimize ambient exposure. All measurements were conducted in a cryogenic probe station fitted with an optical fiber, following the protocol described in the Methods section and earlier literature [13, 17, 41]. The current–voltage (I–V) characteristics of an MSM photodiode resemble that of two reverse-biased Schottky diodes that are connected in series (Fig. 3(a)). Voltage biases were limited to 15 V to avoid irreversible breakdown. At low biases, the current is limited by the reverse saturation current of the Schottky diode at the source (drain) electrode for positive (negative) drain voltage biases (Fig. 3(a)). Consequently, the dark current of Bi_2O_2Se photodiodes remains below 0.2 nA for applied biases up to 7 V at 7 K and then begins to increase due to the onset of avalanche breakdown (Figs. 3(b) and 3(c)). Under illumination at $\lambda = 515.6$ nm, the device shows normal Schottky diode behavior up to 2.1 V with an increased reverse saturation current (I_{sat}) of 20 nA due to photogenerated excess carriers in the depletion region (Figs. 3(b) and 3(c)). For biases above 2.1 V, the avalanche process becomes dominant, resulting in the current increasing rapidly with bias, as marked by regime (II) in Fig. 3(c). Here, the photocurrent (I_{pc}) is characterized by the multiplication factor, $M = I_{pc}/I_{sat}$, which increases up to ~ 400 at 7 V. At biases

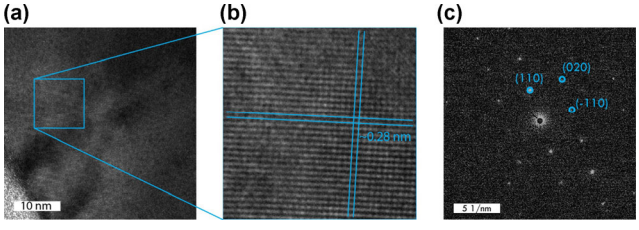

Figure 2 (a) Low-magnification TEM image of the Bi_2O_2Se single crystal. (b) Atomic-resolution TEM image showing the expected lattice spacing of 0.28 nm. (c) SAED pattern showing symmetry points of the single crystal. The TEM analysis is in agreement with literature precedent [28].

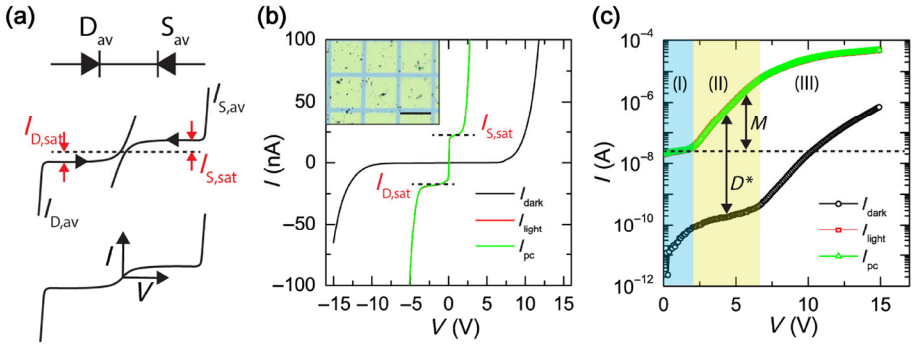

Figure 3 (a) Schematic of the Bi_2O_2Se photodetector with two Schottky diodes near the source (S_{AV}) and drain (D_{AV}) metal contacts and corresponding I–V characteristics of the individual Schottky diodes. $I_{D,sat}$ and $I_{S,sat}$ are reverse saturation currents, and $I_{D,av}$ and $I_{S,av}$ are avalanche currents for the drain and source Schottky diodes, respectively. (b) Current–voltage (I–V) characteristics of a bulk Bi_2O_2Se photodetector at 7 K in the dark (I_{dark}) and under illumination (I_{light}) at an intensity of P = 5.12 mW/cm^2 (I_{pc} = I_{light} − I_{dark}). I_{light} and I_{pc} curves are overlapping. Horizontal dashed lines show reverse saturation currents for the two Schottky diodes under illumination. The inset shows an optical image of the devices (scale bar = 30 μm). (c) I–V characteristics on a log-linear scale showing the three regimes of the avalanche photodetector: (I) normal reverse-biased Schottky diode; (II) avalanche process characterized by an increase in photocurrent; (III) Geiger mode characterized by an increase in the dark current. The multiplication factor M is defined by the ratio of photocurrent in the regimes (II) and (I). Detectivity D^* increases monotonically with the ratio of photocurrent and dark current in regime (II).

larger than 7 V, the device enters the Geiger mode, where the dark current also undergoes the avalanche process. The asymmetry in the I–V characteristics is due to different Schottky barrier heights at the drain and source contacts (Fig. 3(b)).

Bi_2O_2Se APDs empirically show the following multiplication factor behavior: $M = \dfrac{1}{1-\left(V/V_b\right)^n}$, which can be rewritten as $\ln(1-1/M) = n(\ln(V) - \ln(V_b))$, where n is the ideality factor, and V_b is the breakdown voltage. Under illumination, the photodiodes show n = 2 in the avalanche regime (Fig. 4(a)). However, the avalanche breakdown under no illumination empirically possesses a larger value of n = 5 due to the reduced density of primary carriers initiating the avalanche process (Fig. 4(b)) [10, 38]. Since the density of primary carriers is enhanced at higher illumination intensity, the avalanche onset voltage is also reduced (Fig. 4(c)). Figure 5(a) shows the intensity dependence of responsivity in three regimes labeled (I), (II), and (III). In regime (I), the reverse saturation current increases linearly with intensity ($I_{pc} \sim P^{\gamma}$, $\gamma \sim 1$) due to excess photocarriers in the depletion region, resulting in intensity-independent responsivity since $R \sim I_{pc}/P$ (Fig. 5(a)) [10, 38]. Avalanche photocurrent in regime (II) shows $\gamma \sim 0.65$ ($R \sim P^{-0.35}$) with the highest multiplication gain (~ 400) being achieved at 7 V for the highest intensity of 5.12 mW/cm^2, which implies a responsivity of ~ 563 A/W. At 7 V, the highest responsivity of $R \sim 3 \times 10^3$ A/W is achieved concurrently with the lowest dark current of 0.2 nA at $P = 4.5 \times 10^{-5}$ W/cm^2 (Figs. 5(a) and 3(c)). Thus, the gain or internal quantum efficiency (i.e., total number of generated charge carriers divided by the total number of incident photons) is ~ 7.3×10^3. Even higher responsivity up to ~ 6.9×10^4 A/W can be achieved in regime (III) at 15 V ($\gamma \sim 0.4$, $R \sim P^{-0.6}$), but the tradeoff is a much larger dark current (~ 0.8 μA) that decreases detectivity, as will be discussed further below (Figs. 5(a) and 3(c)). Monotonically decreasing γ with increasing applied voltage signifies increased bimolecular recombination losses in reverse biased Schottky diodes.

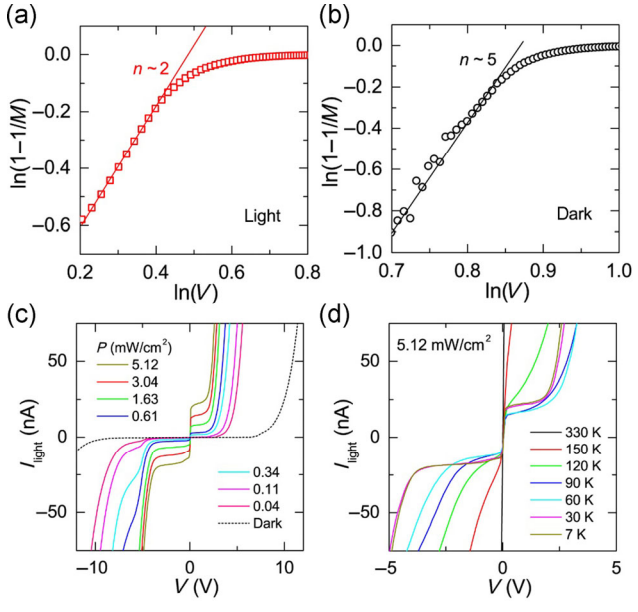

Figure 4 (a) and (b) Plots of ln(1 − 1/M) versus log(V) showing the avalanche process with a power factor of n = 2 and n = 5 under illumination (P = 5.12 mW/cm^2) and in the dark, respectively. (c) I–V characteristics of the photodetector at 7 K and under different illumination intensities. (d) I–V characteristics of the photodetector at P = 5.12 mW/cm^2 at different temperatures.

Varying the temperature during operation provides further insight into the photocurrent generation mechanism. At room temperature, Bi_2O_2Se MSM devices show quasi-ohmic behavior in the dark and slightly super-linear I–V characteristics under illumination due to charge injection from the contacts (Fig. S3(a) in the ESM) [11]. The dark current decreases rapidly with reducing temperature at low biases, allowing a thermionic emission model to extract a Schottky barrier height of 43.8 meV (Figs. S3(b) and S4 in the ESM). I–V characteristics under illumination also show a transition from quasi-ohmic behavior to the emergence of reverse saturation current between 150 and 90 K (Fig. 4(d)). As expected, the reverse saturation current does not change below 90 K where the thermal generation of carriers is expected to freeze-out (Fig. 4(d)) [10]. In addition, the avalanche process initiates at smaller biases at lower temperatures due to decreased contribution from competing thermionic emission. The dark and light I–V characteristics show a power law behavior $I_{dark} \sim V^m$ (maximum m ~ 10 at 7 K) at voltages higher than 7 V due to the emergence of the avalanche process at ~ 120 K (Figs. S3(b) and S5 in the ESM). As expected, Bi_2O_2Se avalanche photodiodes under illumination

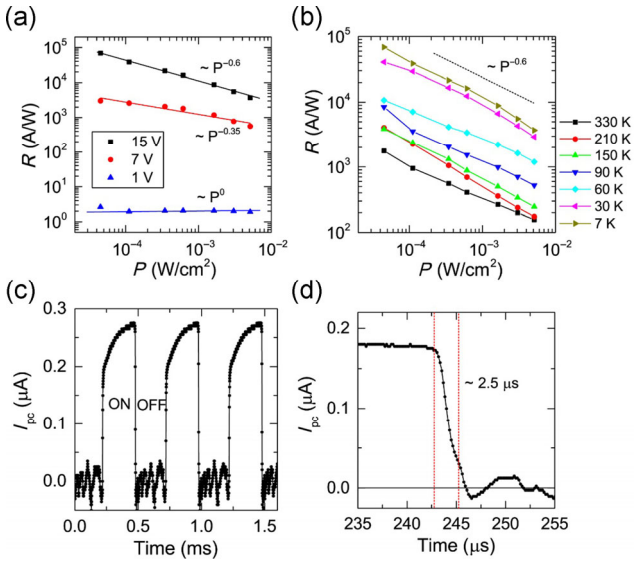

Figure 5 (a) Plot of responsivity (R) versus illumination intensity (P) for the Bi_2O_2Se photodiode biased in regimes (I) (1 V), (II) (7 V), and (III) (15 V) at 7 K. (b) R versus P plot measured at V = 15 V at different temperatures. (c) Temporal response of the Bi_2O_2Se photodetector (V = 7 V) while the light (P = 5.12 mW/cm^2) is modulated using an electronic chopper at a frequency of 2 kHz. (d) The zoomed-in plot of the photocurrent profile showing a decay time of 2.5 μs.

show a positive temperature coefficient of resistance at low temperatures (T < 250 K), where competing thermionic emission becomes less effective (Fig. S6 in the ESM). A power-law behavior with m > 2 has also been associated with space-charge-limited current for an exponential distribution of trap states that modify the Mott-Gurney relation ($I \sim V^2/L^3$) to $I \sim V^m/L^{2m-1}$ with exponent, $m = 1 + T_c/T$; where, L is the channel length and T_c is the characteristic temperature of traps [42–45]. Thus, for typical low mobility disordered systems, m > 2 for T < T_c and trap states begin to fill up at high biases. In single crystal Bi_2O_2Se devices, however, this mechanism can be ruled out because the family of curves at different temperatures, either in dark (Fig. S3(b) in the ESM) or under light (Fig. S5(a) in the ESM), do not intersect at a common point where all of the traps would be filled.

To illustrate this point further, we compare our single-crystal Bi_2O_2Se results with charge transport in composite films of Bi_2O_2Se flakes that intentionally have a large density of trap states resulting from the disordered nature of percolating composite films. In this case, Bi_2O_2Se flakes (average thickness of 50 nm) were liquid-phase exfoliated and reassembled in thin films (see Fig. S7(a) in the ESM). I–V characteristics of these films at variable temperatures in dark show $I \sim V^m$ (Fig. S7(b) in the ESM), where the temperature dependence of m shows excellent agreement with theory (inset of Fig. S7(b) in the ESM). Moreover, the power-law behavior of the family of curves can be extrapolated to meet at a single point (V_c = 160 V) where all trap states are expected to be filled. Similar behavior has also been reported in other disordered layered materials such as composite films of reduced graphene oxide [46]. Furthermore, as expected, the trap states can also be filled by optical illumination (P = 5.12 mW/cm^2) where the resulting I–V curves become relatively parallel (Fig. S7(c) in the ESM). In contrast, extrapolation of the I–V curves of single-crystal Bi_2O_2Se devices tends to intersect at multiple points (Figs. S3(b) and S5(a) in the ESM). Overall, these observations combined with the excellent fit of the carrier multiplication model in Figs. 4(a) and 4(b) rule out trap filling processes.

Zener breakdown tunneling can also be ruled out due to the absence of exponential I–V characteristics [10]. It should be noted that Zener breakdown inter-band tunneling is typically observed in reverse-biased p-n heterojunction diodes that employ highly doped semiconductors [10]. However, Hall measurements of the Bi_2O_2Se crystal show low electron doping in the range of 10^{15}–10^{16} cm^{-3} at room temperature, which is orders of magnitude smaller than required for Zener breakdown. In addition, the intensity dependence of responsivity follows the same power law behavior at all temperatures since the role of temperature in photocarrier generation is solely via dark current modulation (Fig. 5(b)).

Photodetector detectivity (D^*) is defined as $D^* = R(A)^{0.5}/i_N$, where A is the area of the device (1.5×10^{-6} cm^2) and i_N is the noise current. Assuming the shot noise limit at 7 K, $i_N = (2eI_{dark})^{0.5} = 8 \times 10^{-15}$ A/Hz. Then, D^* increases rapidly with voltage in the avalanche regime (as indicated by the arrow in Fig. 3(c)). The maximum value of D^* for Bi_2O_2Se APDs at 7 V is found to be ~ 4.6×10^{14} Jones, which is the highest value reported for any layered semiconductor [1, 3, 4]. The temporal response of the Bi_2O_2Se photodiodes is further probed through electronic modulation of the laser illumination (P = 5.12 mW/cm^2) while the device was biased at 7 V to keep the device in the avalanche regime (II) (Figs. 5(c) and 5(d)). The characteristic time constant (defined by 80% decay in the photocurrent) is found to be 2.5–3.5 μs, which is limited by the instrumentation response (Fig. 5(d)). The photocurrent rise has a longer time constant of ~ 100 μs that is not present in the decay process, possibly due to vastly different defect trapping and de-trapping rates. Overall, we obtain an intrinsic gain of 7.3×10^3 and bandwidth of ~ 400 kHz, which implies a gain bandwidth product in the range ~ 2.1–2.9 GHz, again one of the highest values reported for layered materials [1, 3, 4].

These Bi_2O_2Se photodiodes show the avalanche effect up to 90 K (Fig. 4(d)) that is limited by the Schottky barrier height (~ 44 meV) with Au electrodes, although the operating temperature can be further increased by designing larger Schottky barrier heights using different metals. The high intrinsic photodetection gain likely results from a combination of different factors such as the indirect bandgap of Bi_2O_2Se, an optical excitation energy (~ 2.37 eV) that is larger than twice the bandgap (~ 0.8 eV), and the favorable competition between impact ionization and phonon-induced hot carrier relaxation in Bi_2O_2Se.

Another indicator of favorable impact ionization is weak electron–phonon coupling. Electron–phonon coupling, which is expected to counteract carrier multiplication, is frequently observed to be weak in thermoelectric materials such as PbSe and PbTe [47, 48]. Bi_2O_2Se, which is calculated to be an excellent high-temperature n-type thermoelectric material with figure-of-merit (zT) of 3.35 in doping-optimized nanosheets [49], shows similar electron–phonon coupling behavior. The influence of electron–phonon coupling is captured in the deformation potential (Ξ), which can be estimated using the single parabolic band approximation [47], $\mu_0 = \pi e\hbar^4 C_l / \sqrt{2} m_I^* (m_b^* k_B T)^{3/2} \Xi^2$. Here, e is the fundamental electronic charge, $\hbar$ is Planck's constant, k_B is Boltzmann's constant, T is temperature, C_l is the longitudinal elastic constant, m_b^* is the band effective mass, and m_I^* is the inertial effective mass of electrons in Bi_2O_2Se.

μ_0 is a Drude mobility factor calculated from the following expression: $\sigma_{E_0} = \frac{8\pi e(2m_e k_B T)^{3/2}}{3h^3} \cdot \mu_0 \left(\frac{m_S^*}{m_e}\right)^{3/2}$, where m_e is electron mass, m_S^* is the Seebeck effective mass, and σ_{E_0} is found directly from thermoelectric property measurements [47, 50]. We measure a Hall mobility of $\mu_H \approx 20$ cm^2/(V·s) at room temperature in the Bi_2O_2Se crystals prepared for this study. By taking values of m_I^* from Ref. [49], m_b^*, carrier density, and Seebeck coefficient from Ref. [51], and C_l from Ref. [52], we calculate $\Xi \approx 33$ eV. On other hand, by taking longitudinal effective mass (m_a) from a recent report of Bi_2O_2Se in Ref. [28], we calculate $m_I^* = 3\left(\frac{2}{m_a^*} + \frac{1}{m_c}\right)^{-1}$, where m_c is obtained from $m_b^* = \left(m_a^2.m_c\right)^{1/3}$ from Ref. [51], resulting in $\Xi \approx 27$ eV. We note that the estimate of Ξ in the range of 27–33 eV depends on various values of effective masses, elastic constants, and thermoelectric measurements extracted from theoretical and experimental studies on samples with different doping levels with dominant acoustic phonon scattering behavior [28, 49, 51, 52]. Nevertheless, Ξ for Bi_2O_2Se is comparable to high-performance thermoelectric materials such as PbSe-n ($\Xi \approx$ 25 eV), PbSe-p ($\Xi \approx 35$ eV), PbTe-n ($\Xi \approx 22$ eV), and PbTe-p ($\Xi \approx 25$ eV), suggesting that similarly weak electron–phonon coupling is playing a favorable role in impact ionization in Bi_2O_2Se photodiodes [48]. Further understanding of the hot carrier relaxation pathways competing with the avalanche process can be discerned from first-principles calculations, ultrafast transient spectroscopy, and temperature-dependent thermoelectric measurements within the acoustic phonon scattering regime [48, 53].

3 Conclusions

In conclusion, we studied intrinsic carrier multiplication processes in avalanche photodiodes fabricated from Au Schottky metal contacts on Bi_2O_2Se semiconducting crystals. The indirect and near-infrared bandgap of Bi_2O_2Se facilitates impact ionization under visible excitation, producing the highest carrier multiplication factor (> 400) and internal quantum efficiency (> 7,000) that exceed all other layered semiconductors. The intrinsic carrier multiplication mechanism enables concurrent improvement in all relevant photodetector metrics, resulting in a gain bandwidth product in excess of 1 GHz. The multiplication process within the depletion region near the Au contacts is understood through variable temperature and illumination intensity measurements within a standard avalanche breakdown model. Overall, this work establishes Bi_2O_2Se as a leading layered semiconductor candidate for photodetector applications.

4 Methods

4.1 Chemical vapor transport growth of Bi_2O_2Se crystals

Bismuth (99.9999%) and bismuth oxide (99.9998%) were obtained from Strem, USA, and selenium (99.999%) was obtained from Sigma-Aldrich, Czech Republic. For the crystal growth, quartz glass ampoules were used with alumina crucible liners. Stochiometric amounts of bismuth, bismuth oxide, and selenium corresponding to 15 g of Bi_2O_2Se were placed in the alumina crucible inside of the quartz ampoule, after which the quartz ampoule was melt sealed under high vacuum (10^{-3} Pa). The bismuth oxide was used in 1 wt.% excess over stoichiometry to compensate for its reaction with the alumina liner. The ampoule was heated to 1,000 °C using a 5 °C/min heating rate. After 1 h at 1,000 °C, the ampoule was cooled to 730 °C over a period of 24 h. After 48 h at 730 °C, the ampoule was freely cooled to room temperature.

4.2 X-ray photoelectron spectroscopy

XPS measurements were performed on a high vacuum Thermo Scientific ESCALAB 250 Xi+ XPS system at a base pressure of ~ 10^{-8} Torr using an Al Kα X-ray source (~ 1,486.6 eV) with a 900 μm spot size and a 0.1 eV binding energy resolution. All subpeaks were fit using the software suite Avantage (Thermo Scientific), as shown in Fig. S2 in the ESM. In the case of Bi 4f and Se 3d, the peaks were fitted using doublets. The dominant peaks in all spectra agree with literature precedent [28].

4.3 Bi_2O_2Se avalanche photodetector measurements

All Bi_2O_2Se APD photocurrent measurements were carried out using a LakeShore CRX 4K cryogenic probe station (pressure < 5 × 10^{-4} Torr at room temperature and pressure ~ 10^{-7} Torr at 7 K). Current–voltage characteristics were measured using two Keithley 2400 source-meters controlled by home-written LabVIEW programs. All photocurrent measurements were performed using a fiber-coupled laser diode with excitation wavelength of 515.6 nm (LP520MF100, Thor Labs). The local illumination intensity was calibrated with a Si detector. The temporal response was obtained by using an internal oscillator in the laser controller (ITC4001, Thor Labs).

Acknowledgments

This research was supported by the Materials Research Science and Engineering Center (MRSEC) of Northwestern University (NSF DMR-1720139). Z. S. and J. L. were supported by project LTAUSA19034 from the Ministry of Education Youth and Sports (MEYS). J. P. M. and G. J. S. acknowledge Award 70NANB19H005 from U.S. Department of Commerce, National Institute of Standards and Technology as part of the Center for Hierarchical Materials Design (CHiMaD).

Electronic Supplementary Material: Supplementary material (additional details of the materials characterization and photocurrent measurements) is available in the online version of this article at https://doi.org/10.1007/s12274-020-3059-3.

REFERENCES

[1] Koppens, F. H. L.; Mueller, T.; Avouris, P.; Ferrari, A. C.; Vitiello, M. S.; Polini, M. Photodetectors based on graphene, other two-dimensional materials and hybrid systems. *Nat. Nanotechnol.* **2014**, *9*, 780–793.

[2] Sangwan, V. K.; Hersam, M. C. Electronic transport in two-dimensional materials. *Annu. Rev. Phys. Chem.* **2018**, *69*, 299–325.

[3] Konstantatos, G.; Sargent, E. H. Nanostructured materials for photon detection. *Nat. Nanotechnol.* **2010**, *5*, 391–400.

[4] Sun, Z. H.; Chang, H. X. Graphene and graphene-like two-dimensional materials in photodetection: Mechanisms and methodology. *ACS Nano* **2014**, *8*, 4133–4156.

[5] Beck, M. E.; Hersam, M. C. Emerging opportunities for electrostatic control in atomically thin devices. *ACS Nano* **2020**, *14*, 6498–6518.

[6] Padgaonkar, S.; Olding, J. N.; Lauhon, L. J.; Hersam, M. C.; Weiss, E. A. Emergent optoelectronic properties of mixed-dimensional heterojunctions. *Acc. Chem. Res.* **2020**, *53*, 763–772.

[7] Sangwan, V. K.; Hersam, M. C. Neuromorphic nanoelectronic materials. *Nat. Nanotechnol.* **2020**, *15*, 517–528.

[8] Jariwala, D.; Sangwan, V. K.; Lauhon, L. J.; Marks, T. J.; Hersam, M. C. Emerging device applications for semiconducting two-dimensional transition metal dichalcogenides. *ACS Nano* **2014**, *8*, 1102–1120.

[9] Furchi, M. M.; Polyushkin, D. K.; Pospischil, A.; Mueller, T. Mechanisms of photoconductivity in atomically thin MoS_2. *Nano Lett.* **2014**, *14*, 6165–6170.

[10] Sze, S. M.; Ng, K. K. *Physics of Semiconductor Devices*; John Wiley & Sons: New York, 2006.

[11] Bube, R. H. *Photoelectronic Properties of Semiconductors*; Cambridge University Press: Cambridge, 1992.

[12] Fang, H. H.; Hu, W. D. Photogating in low dimensional photodetectors. *Adv. Sci.* **2017**, *4*, 1700323.

[13] Kang, J.; Wells, S. A.; Sangwan, V. K.; Lam, D.; Liu, X. L.; Luxa, J.; Sofer, Z.; Hersam, M. C. Solution-based processing of optoelectronically active indium selenide. *Adv. Mater.* **2018**, *30*, 1802990.

[14] Zhang, W. J.; Chuu, C. P.; Huang, J. K.; Chen, C. H.; Tsai, M. L.; Chang, Y. H.; Liang, C. T.; Chen, Y. Z.; Chueh, Y. L.; He, J. H. et al. Ultrahigh-gain photodetectors based on atomically thin graphene-MoS_2 heterostructures. *Sci. Rep.* **2014**, *4*, 3826.

[15] Kufer, D.; Konstantatos, G. Highly sensitive, encapsulated MoS_2 photodetector with gate controllable gain and speed. *Nano Lett.* **2015**, *15*, 7307–7313.

[16] Choi, W.; Cho, M. Y.; Konar, A.; Lee, J. H.; Cha, G. B.; Hong, S. C.; Kim, S.; Kim, J.; Jena, D.; Joo, J. et al. High-detectivity multilayer MoS_2 phototransistors with spectral response from ultraviolet to infrared. *Adv. Mater.* **2012**, *24*, 5832–5836.

[17] Kang, J.; Sangwan, V. K.; Lee, H. S.; Liu, X. L.; Hersam, M. C. Solution-processed layered gallium telluride thin-film photodetectors. *ACS Photonics* **2018**, *5*, 3996–4002.

[18] Wu, C. C.; Jariwala, D.; Sangwan, V. K.; Marks, T. J.; Hersam, M. C.; Lauhon, L. J. Elucidating the photoresponse of ultrathin MoS_2 field-effect transistors by scanning photocurrent microscopy. *J. Phys. Chem. Lett.* **2013**, *4*, 2508–2513.

[19] Konstantatos, G.; Badioli, M.; Gaudreau, L.; Osmond, J.; Bernechea, M.; de Arquer, F. P. G.; Gatti, F.; Koppens, F. H. L. Hybrid graphene-quantum dot phototransistors with ultrahigh gain. *Nat. Nanotechnol.* **2012**, *7*, 363–368.

[20] Duan, N.; Liow, T. Y.; Lim, A. E. J.; Ding, L.; Lo, G. Q. 310 GHz gain-bandwidth product Ge/Si avalanche photodetector for 1550 nm light detection. *Opt. Exp.* **2012**, *20*, 11031–11036.

[21] Farrell, A. C.; Meng, X.; Ren, D. K.; Kim, H.; Senanayake, P.; Hsieh, N. Y.; Rong, Z. X.; Chang, T. Y.; Azizur-Rahman, K. M.; Huffaker, D. L. InGaAs–GaAs nanowire avalanche photodiodes toward single-photon detection in free-running mode. *Nano Lett.* **2019**, *19*, 582–590.

[22] Lei, S. D.; Wen, F. F.; Ge, L. H.; Najmaei, S.; George, A.; Gong, Y. J.; Gao, W. L.; Jin, Z. H.; Li, B.; Lou, J. et al. An atomically layered InSe avalanche photodetector. *Nano Lett.* **2015**, *15*, 3048–3055.

[23] Dastgeer, G.; Khan, M. F.; Nazir, G.; Afzal, A. M.; Aftab, S.; Naqvi, B. A.; Cha, J.; Min, K. A.; Jamil, Y.; Jung, J. et al. Temperature-dependent and gate-tunable rectification in a black phosphorus/WS_2 van der Waals heterojunction diode. *ACS Appl. Mater. Interfaces* **2018**, *10*, 13150–13157.

[24] Gao, A. Y.; Lai, J. W.; Wang, Y. J.; Zhu, Z.; Zeng, J. W.; Yu, G. L.; Wang, N. Z.; Chen, W. C.; Cao, T. J.; Hu, W. D. et al. Observation of ballistic avalanche phenomena in nanoscale vertical InSe/BP heterostructures. *Nat. Nanotechnol.* **2019**, *14*, 217–222.

[25] Ahmed, F.; Kim, Y. D.; Yang, Z.; He, P.; Hwang, E.; Yang, H.; Hone, J.; Yoo, W. J. Impact ionization by hot carriers in a black phosphorus field effect transistor. *Nat. Commun.* **2018**, *9*, 3414.

[26] Pak, J.; Jang, Y.; Byun, J.; Cho, K.; Kim, T. Y.; Kim, J. K.; Choi, B. Y.; Shin, J.; Hong, Y.; Chung, S. et al. Two-dimensional thickness-dependent avalanche breakdown phenomena in MoS_2 field-effect transistors under high electric fields. *ACS Nano* **2018**, *12*, 7109–7116.

[27] Wu, J. X.; Tan, C. W.; Tan, Z. J.; Liu, Y. J.; Yin, J. B.; Dang, W. H.; Wang, M. Z.; Peng, H. L. Controlled synthesis of high-mobility atomically thin bismuth oxyselenide crystals. *Nano Lett.* **2017**, *17*, 3021–3026.

[28] Wu, J. X.; Yuan, H. T.; Meng, M. M.; Chen, C.; Sun, Y.; Chen, Z. Y.; Dang, W. H.; Tan, C. W.; Liu, Y. J.; Yin, J. B. et al. High electron mobility and quantum oscillations in non-encapsulated ultrathin semiconducting Bi_2O_2Se. *Nat. Nanotechnol.* **2017**, *12*, 530–534.

[29] Luu, S. D. N.; Vaqueiro, P. Layered oxychalcogenides: Structural chemistry and thermoelectric properties. *J. Mater.* **2016**, *2*, 131–140.

[30] Harada, J. K.; Charles, N.; Poeppelmeier, K. R.; Rondinelli, J. M. Heteroanionic materials by design: Progress toward targeted properties. *Adv. Mater.* **2019**, *31*, 1805295.

[31] Chen, C.; Wang, M. X.; Wu, J. X.; Fu, H. X.; Yang, H. F.; Tian, Z.; Tu, T.; Peng, H.; Sun, Y.; Xu, X. et al. Electronic structures and unusually robust bandgap in an ultrahigh-mobility layered oxide semiconductor, Bi_2O_2Se. *Sci. Adv.* **2018**, *4*, eaat8355.

[32] Fu, H. X.; Wu, J. X.; Peng, H. L.; Yan, B. H. Self-modulation doping effect in the high-mobility layered semiconductor Bi_2O_2Se. *Phys. Rev. B* **2018**, *97*, 241203.

[33] Fu, Q. D.; Zhu, C.; Zhao, X. X.; Wang, X. L.; Chaturvedi, A.; Zhu, C.; Wang, X. W.; Zeng, Q. S.; Zhou, J. D.; Liu, F. C. et al. Ultrasensitive 2D Bi_2O_2Se phototransistors on silicon substrates. *Adv. Mater.* **2019**, *31*, 1804945.

[34] Li, J.; Wang, Z. X.; Wen, Y.; Chu, J. W.; Yin, L.; Cheng, R. Q.; Lei, L.; He, P.; Jiang, C.; Feng, L. P. et al. High-performance near-infrared photodetector based on ultrathin Bi_2O_2Se nanosheets. *Adv. Funct. Mater.* **2018**, *28*, 1706437.

[35] McKay, K. G. Avalanche breakdown in silicon. *Phys. Rev.* **1954**, *94*, 877–884.

[36] Miller, S. L. Avalanche breakdown in germanium. *Phys. Rev.* **1955**, *99*, 1234–1241.

[37] Miller, S. L. Ionization rates for holes and electrons in silicon. *Phys. Rev.* **1957**, *105*, 1246–1249.

[38] Wolff, P. A. Theory of electron multiplication in silicon and germanium. *Phys. Rev.* **1954**, *95*, 1415–1420.

[39] Sparks, M.; Mills, D. L.; Warren, R.; Holstein, T.; Maradudin, A. A.; Sham, L. J.; Loh, E., Jr; King, D. F. Theory of electron-avalanche breakdown in solids. *Phys. Rev. B* **1981**, *24*, 3519–3536.

[40] Werner, J. H.; Kolodinski, S.; Queisser, H. J. Novel optimization principles and efficiency limits for semiconductor solar cells. *Phys. Rev. Lett.* **1994**, *72*, 3851–3854.

[41] Wells, S. A.; Henning, A.; Gish, J. T.; Sangwan, V. K.; Lauhon, L. J.; Hersam, M. C. Suppressing ambient degradation of exfoliated InSe nanosheet devices via seeded atomic layer deposition encapsulation. *Nano Lett.* **2018**, *18*, 7876–7882.

[42] Lampert, M. A. Simplified theory of space-charge-limited currents in an insulator with traps. *Phys. Rev.* **1956**, *103*, 1648–1656.

[43] Rose, A. Space-charge-limited currents in solids. *Phys. Rev.* **1955**, *97*, 1538–1544.

[44] Ghatak, S.; Ghosh, A. Observation of trap-assisted space charge limited conductivity in short channel MoS_2 transistor. *Appl. Phys. Lett.* **2013**, *103*, 122103.

[45] Kumar, V.; Jain, S. C.; Kapoor, A. K.; Poortmans, J.; Mertens, R. Trap density in conducting organic semiconductors determined from temperature dependence of *J–V* characteristics. *J. Appl. Phys.* **2003**, *94*, 1283–1285.

[46] Joung, D.; Chunder, A.; Zhai, L.; Khondaker, S. I. Space charge limited conduction with exponential trap distribution in reduced graphene oxide sheets. *Appl. Phys. Lett.* **2010**, *97*, 093105.

[47] Zevalkink, A.; Smiadak, D. M.; Blackburn, J. L.; Ferguson, A. J.; Chabinyc, M. L.; Delaire, O.; Wang, J.; Kovnir, K.; Martin, J.; Schelhas, L. T. et al. A practical field guide to thermoelectrics: Fundamentals, synthesis, and characterization. *Appl. Phys. Rev.* **2018**, *5*, 021303.

[48] Wang, H.; Pei, Y. Z.; LaLonde, A. D.; Snyder, G. J. Weak electron–phonon coupling contributing to high thermoelectric performance in n-type PbSe. *Proc. Natl. Acad. Sci. USA* **2012**, *109*, 9705–9709.

[49] Yu, J. B.; Sun, Q. Bi_2O_2Se nanosheet: An excellent high-temperature n-type thermoelectric material. *Appl. Phys. Lett.* **2018**, *112*, 053901.

[50] Borup, K. A.; Toberer, E. S.; Zoltan, L. D.; Nakatsukasa, G.; Errico, M.; Fleurial, J. P.; Iversen, B. B.; Snyder, G. J. Measurement of the electrical resistivity and Hall coefficient at high temperatures. *Rev. Sci. Instrum.* **2012**, *83*, 123902.

[51] Drasar, C.; Ruleova, P.; Benes, L.; Lostak, P. Preparation and transport properties of Bi_2O_2Se single crystals. *J. Electron. Mater.* **2012**, *41*, 2317–2321.

[52] Tan, X.; Liu, Y. C.; Hu, K. R.; Ren, G. K.; Li, Y. M.; Liu, R.; Lin, Y. H.; Lan, J. L.; Nan, C. W. Synergistically optimizing electrical and thermal transport properties of Bi_2O_2Se ceramics by Te-substitution. *J. Am. Ceram. Soc.* **2018**, *101*, 326–333.

[53] Zhong, C. M.; Sangwan, V. K.; Kang, J.; Luxa, J.; Sofer, Z.; Hersam, M. C.; Weiss, E. A. Hot carrier and surface recombination dynamics in layered InSe crystals. *J. Phys. Chem. Lett.* **2019**, *10*, 493–499.